ZDES of an Ariane 6 PPH configuration with incidence angle using Zonal Immersed Boundary Conditions

Pierre-Elie Weiss

DOI: 10.13009/EUCASS2019-274

ZDES of an Ariane 6 PPH configuration with incidence angle using Zonal Immersed Boundary Conditions

P. E. Weiss⋆
⋆*ONERA - The French Aerospace Lab, F-92190, Meudon, France*

Abstract

A numerical framework denoted as Zonal Immersed Boundary Conditions (ZIBC) has recently been developed and successfully applied to a full space launcher model namely Ariane 5 (see Weiss and Deck[34]). One of the next development step lies in the validation and the extension of this methodology for different configurations. In particular, the robustness of the approach needs to be confirmed for unsteady numerical simulations using ZDES which is the objective of the present paper. To do so, a sub-scale Ariane 6 PPH model is computed for two transonic Mach numbers (i.e. $M_\infty = 0.7$ and 0.9) with an angle of attack equal to $-3°$. In this case, the sting holding the model, the main stage and the boosters consisting in cylindrical bodies with changing areas are modelled using a classical body-fitted (BF) approach. Then, the struts linking the main stage to the boosters are reproduced by the local introduction of immersed boundary conditions as in Mochel et al.[18] and Deck et al.[9] A physical analysis is performed on the basis of the wall fluctuating pressure to investigate the characteristic unsteady phenomena occurring for the specific angle of attack and the near sonic Mach number.

1. Introduction

Simulation tools have reached a sufficient level of maturity to allow the reproduction and the prediction of unsteady aerodynamic phenomena on space vehicles.[3,34] Such a statement is well-illustrated by the long history of studies dedicated to the investigation of the buffeting phenomenom[4,8,11,27,35] following Ariane 5 flight 157 as recently reminded by Saile *et al.*[26] In this context, the present study gives an example of the use of CFD to reproduce and contribute to explain an a priori unexpected unsteady phenomenom which occurs for a very specific regime and angle of attack. This unsteadiness was observed during a test campaign at ONERA's S2MA facility for an intermediate Ariane 6 configuration similar to the one investigated by Pont *et al.*[25]
The objective is here to demonstrate the capacity of the ZIBC (Zonal Immersed Boundary Conditions) approach[16,18,34] coupling ZDES (Zonal Detached Eddy Simulation) and IBC (Immersed Boundary Conditions) to identify and analyse the flow physics of the unsteady flow phenomenon with a limited amount of time devoted to the building of the numerical test case. The first part of the paper details the ZIBC methodology applied to the so-called Ariane 6 PPH case. Then, the first results issued from the ZDES allow to evidence the different instantaneous characteristics of the flow field for the two transonic Mach numbers of interest namely 0.7 and 0.9 which would not have been possible with a steady RANS approach.

2. Description of the test case

The configuration of interest corresponds to a former version of the future Ariane 6 space launcher. Global views of the space vehicle are provided in figure 1. In this figure, the configuration of interest can be decomposed into a central main stage and two boosters linked by two series of struts. The first row of struts (denoted as the forward struts) links the nose cones of the boosters to the main stage. Downstream, the second one (denoted as the aft struts) permits to attach the afterbody bases together. Finally, the sting holding the model (see figure 3(a)) is also taken into account in the simulation to reproduce the blockage effect occurring in the wake.

Two Mach numbers in the transonic regime are considered namely $M_\infty = 0.7$ and $M_\infty = 0.9$ denoted in the following as M07 and M09, respectively. The configuration is inclined by an angle $\alpha = -3°$ so that the flow arrives on the top of the fairing. The detailed sets of parameters related to these two Mach numbers such as the static and stagnation quantities are summarised in table 1.

DOI: 10.13009/EUCASS2019-274

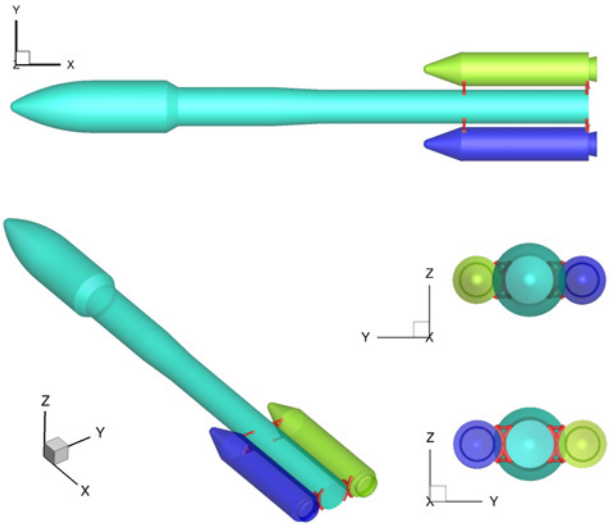

Figure 1: Geometry of the Ariane 6 PPH model

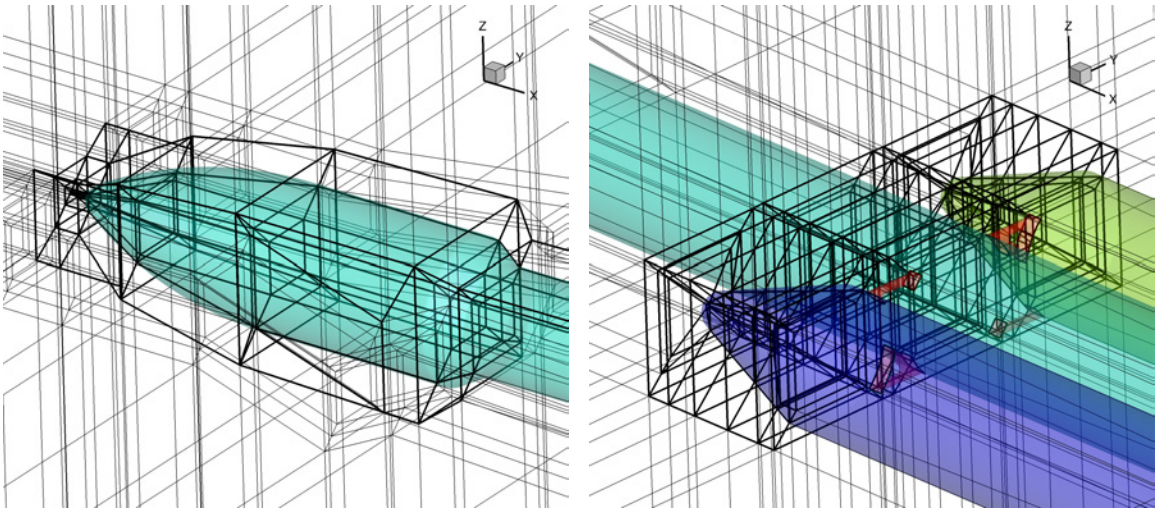

(a) Topology surrounding the fairing

(b) Triple O-H topology

Figure 2: Views of the topology

3. Numerical set-up

The aforementioned freestream conditions lead to a first cell size in the wall normal direction for the two Mach numbers $\Delta y_{0,M07} = 10^{-6}$ m et $\Delta y_{0,M09} = 1.26.10^{-6}$ m which corresponds to a dimensionless first cell size $y^+ = 1$. Given these sizes are close, the lowest cell size is retained allowing to make a common mesh for both cases. A structured multi-block grid is built around the smooth version of the configuration (i.e. limited to the boosters and the main stage without any technological details). The generation of the grid is based on a triple O-H topology (i.e. one O-H topology for each booster and for the main stage) represented in figures 2(a) and 2(b). The resulting mesh constitutes the background grid for the introduction of immersed boundary conditions. Such a topology is designed to avoid singularity problems near the axes.

The whole computational domain consists in a cylinder with a circular section. Its characteristic sizes are willingly high compared to the smallest diameter $D = 0.07$ of the main stage base to avoid any reflections of spurious numerical waves. In practice, the length of the computational domain is approximately equal to $425.5D$ and its diameter equals $400D$ which permits a shift between the area of interest and the boundary of the computational domain equal to $200D$ in the three directions of space.

Knowing the grid refinement in the azimuthal direction often rules the spatial organisation for the azimuthal modes,[8,31,36]

DOI: 10.13009/EUCASS2019-274

Test case	**M07**	**M09**
M_∞ (-)	0.7	0.9
p_∞ (Pa)	169468	109417
T_∞ (K)	282.6	268.1
p_i (Pa)	235000	185000
T_i (K)	310	311
α (deg)	-3	-3
q_∞ (Pa)	58128	62045
$Re_{L_{ref}}$ (-)	3019612	2683383
S_{ref} (m^2)	0.00916	0.00916
L_{ref} (m)	0.108	0.108

Table 1: Geometrical and physical parameters

the number of points must be chosen accordingly. As a consequence, the smooth configuration (without any technological details) clusters 360 points in the azimuthal direction providing 1 degree between two longitudinal planes.
The topology of the mesh, the anisotropy and the asymmetry of the cells (characterized by their skewness) do not take into the incidence of the configuration given the angle of attack is low (i.e. $\alpha = -3°$).
In former studies,[21,32,33] the grid refinement in the confinement zone between the main stage and the boosters was identified as a critical point. Indeed, this resolution seems to be of primary importance to predict the flow reattachment occurring either on a booster or on the main stage. As a consequence, this area is particularly refined in the streamwise and longitudinal directions.
In the end, the mesh is made up with 164 blocks and contains 270×10^6 points. In this background grid thus constituted the technological details namely the struts in the present case are introduced as shown in figure 3.

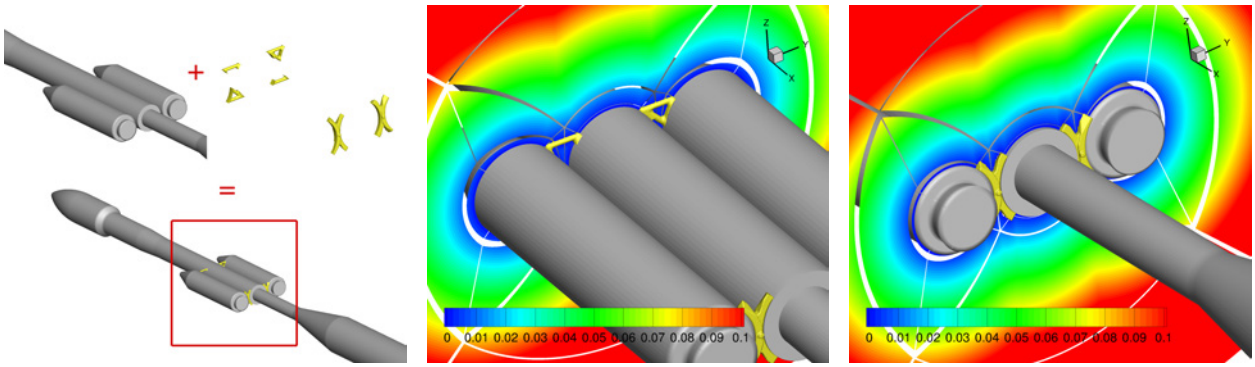

(a) Elements modelled with a body-fitted approach (grey) and Immersed Boundary Conditions (yellow)

(b) Iso-contours of the distance to the wall around the forward struts

(c) Iso-contours of the distance to the wall around the aft struts

Figure 3: Illustration of the ZIBC strategy to take into account the struts in the ZDES of a sub-scale Ariane 6 PPH model

The approach used to take into account complex technological details is the immersed boundary method. Such a

DOI: 10.13009/EUCASS2019-274

method consists in adding body forces in a continuous or discrete manner to mimic classical boundary conditions (e.g. adiabatic or isothermal walls, slip or no-slip conditions, porosity, etc ...). Since the first introduction of the immersed boundary method by Peskin[23] in 1972, the choice of either a continuous or a discrete form of the body forces highly depends on the application at stake (see e.g. Mittal and Iaccarino[17]). For instance, a continuous forcing function introduced in the governing equations before the discretization step appeared more adapted to elastic boundaries.[23,24] Given the rigid bodies considered in the present study and following the conclusions in Goldstein *et al.*[12] and Lai and Peskin,[14] a discrete forcing function has been privileged.

In the present work the continuous form of the compressible Navier-Stokes equations including the ZDES and IBC source terms is summarised. Then, for the sake of brevity, the discrete version of this system, which is implemented in practice, can be found in details in Weiss and Deck[34] for the finite volume approach in the same spirit as in Mohd-Yusof[19] for a spectral approach or Verzicco *et al.*[30] and Fadlun *et al.*[10] for a finite-difference-based LES. The source terms related to the ZDES and the IBC are clearly highlighted in the description of the formulation by the notations $\mathbf{T}^{(1)}_{\mathbf{ZDES}}$ and $\mathbf{T}^{(2)}_{\mathbf{IBC}}$, respectively.

The underlying notion existing behind the coupling between a hybrid RANS/LES method such as ZDES and IBC is a combination of source terms. Writing the integral form of the governing equations, these source terms can be clearly exhibited. In the frame of a finite volume approach, let us consider a finite volume Ω enclosed by a surface $\partial\Omega$ with $\mathbf{n}$ the normal surface vector associated to $d\Sigma$. The Navier-Stokes equations can be written as follows:

$$\frac{\partial}{\partial t}\int_{\Omega}\mathbf{W}d\Omega + \oint_{\partial\Omega}\left(\mathbf{F_c}[\mathbf{W}] - \mathbf{F_d}[\mathbf{W},\nabla\mathbf{W}]\right).\mathbf{n}d\Sigma = \int_{\Omega}\mathbf{T}\left(\mathbf{W},\nabla\mathbf{W}\right)d\Omega \tag{1}$$

where $\mathbf{W}$ is the conservative variable vector, $\mathbf{F_c}$ and $\mathbf{F_d}$ contain the convective and diffusive fluxes respectively and $\mathbf{T} = \mathbf{T}^{(1)}_{\mathbf{ZDES}} + \mathbf{T}^{(2)}_{\mathbf{IBC}}$ denotes the source term. The superscript $\bullet^{(1)}$ indicates that this source term is applied prior to the source term $\bullet^{(2)}$ as it will be discussed in the following.

The Green-Ostrogradski theorem allows to rewrite equation 1 as follows:

$$\frac{\partial}{\partial t}\int_{\Omega}\mathbf{W}d\Omega + \int_{\Omega}\nabla\cdot\left(\mathbf{F_c}[\mathbf{W}] - \mathbf{F_d}[\mathbf{W},\nabla\mathbf{W}]\right)d\Omega = \int_{\Omega}\mathbf{T}\left(\mathbf{W},\nabla\mathbf{W}\right)d\Omega \tag{2}$$

Thus, the integral form of the immersed boundary source term has the following expression, used for the momentum equation and the Spalart-Allmaras transport equation in the present case, to obtain the desired conservative variable vector $\mathbf{W}$:

$$\int_{\Omega}\mathbf{T}^{(2)}_{\mathbf{IBC}}\left(\mathbf{W},\nabla\mathbf{W}\right)d\Omega = \int_{\Omega}\left(\nabla\cdot\left(\mathbf{F_c}[\mathbf{W}] - \mathbf{F_d}[\mathbf{W},\nabla\mathbf{W}]\right) - \mathbf{T}^{(1)}_{\mathbf{ZDES}}\right)d\Omega \tag{3}$$

In the above-mentioned equation, $\mathbf{T}^{(2)}_{\mathbf{IBC}} = \alpha_{IBC}\times\mathbf{f_{IBC}}\left(\mathbf{W},\nabla\mathbf{W}\right)$ with $\alpha_{IBC} = 0$ or 1 depending on whether the considered area is fluid or solid, respectively and $\mathbf{f_{IBC}}$, the forcing function prescribed to obtain the targeted physical properties of the immersed boundaries.

The following form of the Spalart-Allmaras model for compressible flows has been retained as in Deck *et al.*:[7]

$$\frac{\partial\left(\rho\tilde{\nu}\right)}{\partial t} + \nabla\cdot\left(\rho\tilde{\nu}\mathbf{V}\right) = c_{b1}\tilde{S}\rho\tilde{\nu} + \frac{1}{\sigma}\left(\nabla\cdot\left(\left(\mu+\rho\tilde{\nu}\right)\nabla\tilde{\nu}\right) + c_{b2}\nabla\tilde{\nu}\nabla\rho\tilde{\nu}\right) - \rho c_{w1}f_w\left(\frac{\tilde{\nu}}{d_w}\right)^2 \tag{4}$$

where d_w corresponds to the wall distance and the eddy viscosity is defined as $\nu_t = f_{v1}\tilde{\nu}$. Functions f_{v1}, f_{v2} and f_w are near-wall functions of the original RANS turbulence model by Spalart-Allmaras.[29]

The eddy viscosity is finally given by $\mu_t = \rho\nu_t = \rho\tilde{\nu}\dfrac{\left(\frac{\tilde{\nu}}{\nu}\right)^3}{\left(\frac{\tilde{\nu}}{\nu}\right)^3 + 7.1^3}$. The detailed expressions of $\mathbf{W}$, $\mathbf{F_c}$, $\mathbf{F_d}$, $\mathbf{T}^{(1)}_{\mathbf{ZDES}}$ and $\mathbf{T}^{(2)}_{\mathbf{IBC}}$ can also be found in Weiss and Deck.[34]

It can be noticed that a tagging procedure has to be performed distinguishing solid cells from fluid cells. This permits to obtain values of *tagibc* which corresponds to α_{IBC} in the discrete form of the source term $\mathbf{T}^{(2)}_{\mathbf{IBC}}$ and acts as a sensor that reads as:

$$tagibc = \begin{cases} 1 & \text{if the cell center is inside the immersed object} \\ 0 & \text{if the cell center is outside the immersed object} \end{cases} \tag{5}$$

DOI: 10.13009/EUCASS2019-274

A major difference exists between α_{IBC} and *tagibc*. α_{IBC} can be equal to 1 in a part of a cell and equal to 0 in the remaining volume of the same cell. On the contrary, each cell has a value of 0 or 1 for the marker *tagibc*.

In the frame of the Spalart-Allmaras model and thus of ZDES, the accurate calculation of the distance to the wall d_w is crucial (see Eq. 4).

As mentioned before, the use of immersed boundary conditions requires a pre-processing step to distinguish fluid cells (i.e. outside the bodies) from solid cells (i.e. inside the bodies) using a raytracing algorithm such as the one described by O'Rourke[20] from the knowledge of the surface of the technological details which can be made of triangles as in a STL (STereo-Lithography) CAD file. Following the immersion of the object, an update of the wall distance computation has to be performed when a turbulence model needs it (e.g. the Spalart-Allmaras model). First, the distance to the wall d_w^B of the object is computed. During this procedure, the cells inside the geometry are treated as if they were infinitely far from the body. Such a treatment permits to avoid the destruction term in the transport equation of the pseudo-eddy viscosity (Eq. 4) returns negative values for the pseudo-eddy viscosity.[18] In practice, the 'infinite' distance is explicitly set in meters to 10^9 m. Then, the algorithm considers the former wall distances d_w^A corresponding to the geometry without technological detail and modelled with classical boundary conditions. Finally, the minimum between the two distances d_w^A and d_w^B ($d_w = min(d_w^A, d_w^B)$) is preserved and provides the final distance-to-the-wall for the whole configuration.

The selected method consists in a modified approach by Deck[5,6] of the original DES97 (Spalart *et al.*[28]), named Zonal Detached Eddy Simulation (ZDES).

This multi-resolution approach covers the full range of modelling from RANS to LES and aims at treating all classes of flow problems in a single model. To do so, RANS and DES zones are chosen individually. In RANS regions, the model is enforced to behave as a RANS model while in the DES regions, the model can switch from the RANS mode to the LES mode thanks to the following equation:

$$\tilde{d} = \begin{cases} d_w, & mode = 0 \\ \tilde{d}^I_{DES}, & mode = 1 \\ \tilde{d}^{II}_{DES}, & mode = 2 \\ \tilde{d}^{III}_{DES}, & mode = 3 \end{cases} \tag{6}$$

where $\tilde{d}$ stands for the new definition of the hybrid length scale chosen as a function of the nature of the separation. d_w corresponds to the closest distance to the wall. The definitions of $\tilde{d}^I_{DES}$, $\tilde{d}^{II}_{DES}$ and $\tilde{d}^{III}_{DES}$ can be found in Deck.[6] Its advantage lies in the fact that the user can refine the grid in the areas of interest without spoiling the properties of the boundary layer upstream or downstream the separation. The ZDES formulation differs from the DDES and DES97 ones given the functions close to the wall of the RANS model are explicitly nullified in LES mode. The sub-grid length scale is provided by the cubic root of the volume similarly as in classical sub-grid scale models. In practice, the ZDES rapidly switches into LES, limiting the extension to the grey zone responsible for the delay of the formation of the instabilities.
In the frame of the use of Immersed Boundary Conditions, the most automated mode of ZDES namely mode 2 is well-adapted to predict separations for configurations with high pressure and velocity fluctuation downstream.

We have implemented the original IB method (i.e. direct forcing) in two industrial flow solvers namely FLU3M[13] and ONERA's elsA software.[2] Both codes are based on second-order accurate time and space schemes. The calculations presented in this paper are performed with the FLU3M code. This code solves the Navier-Stokes equations with a low-dissipation AUSM+(P) convective scheme[15] on multi-block structured grids without limiter for the M07 case and with a minmod limiter for the M09 case for robustness purposes. The time integration is carried out by means of an implicit second-order accurate backward scheme. Time accuracy of the calculation was checked during the inner iteration process.[22] The simulation was realised on 396 Broadwell cores. The preprocessing needed by the IBC to distinguish mesh cells with a fluid or solid tag is realized by the external program RAYTRACER3D[18] and the Cassiopée modules[1] for FLU3M and elsA, respectively.

4. Instantaneous flow field

The observation of the instantaneous flow field allows to identify qualitatively the spatial organisation of the coherent structures in the turbulent flow. The plot of an isosurface of the dimensionless Q^* criterion represented in figure 4

DOI: 10.13009/EUCASS2019-274

permits to evidence the wide variety of turbulent scales populating the flow. Downstream the separation on the fairing, a classical axisymmetric shear layer grows with a vortex pairing as seen in figure 5 showing iso-contours of the density gradient norm in the booster (B) and no-booster (NB) planes. Then, fully three-dimensional structures form which look like hairpins developing in turbulent boundary layers. The flow reattaches on the main central body before encountering the nose cones of the boosters as well as the forward struts. For the M09 case, expansion waves can be observed in figure 6 which also illustrates in planes between the main stage and each booster that mixing layers develop after the forward struts and interact with the shock system.

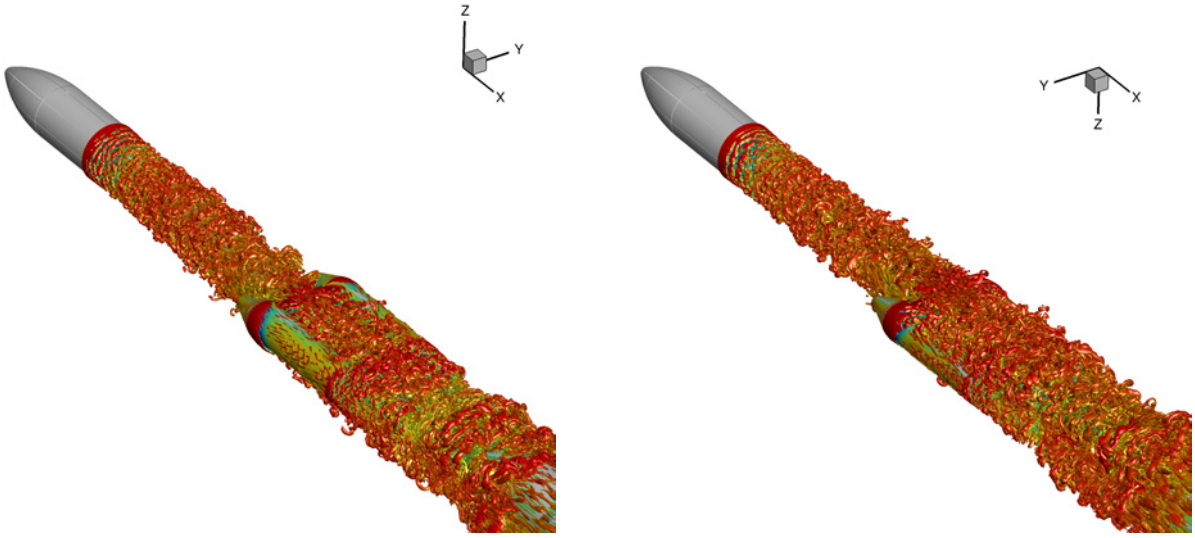

(a) $M_\infty = 0.7$ - Top view

(b) $M_\infty = 0.7$ - Bottom view

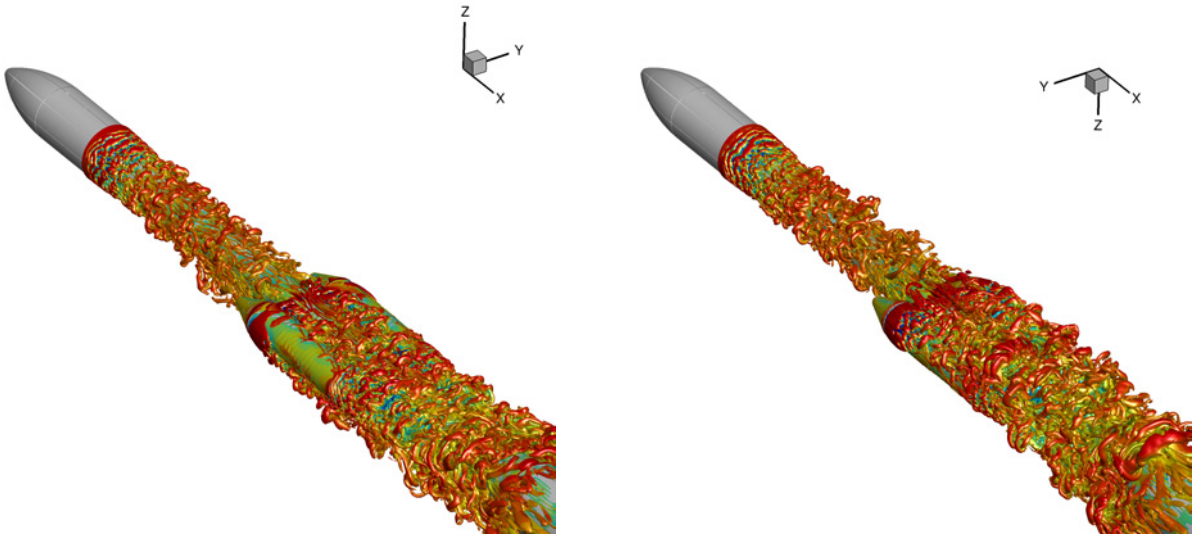

(c) $M_\infty = 0.9$ - Top view

(d) $M_\infty = 0.9$ - Bottom view

Figure 4: Iso-surface of the dimensionless Q^* criterion coloured by the streamwise velocity component ($Q^* = Q^* L_{ref}^2 / U_\infty^2 = 5$)

5. Mean flow analysis

The time-averaged flow field is represented for the pressure coefficient in figure 7. At first sight, the distribution of the mean pressure along the configuration at the wall and in the flow seems to be similar for both Mach numbers. Compression zones are found near the nose cones followed by low pressure areas around the fairing. After the separation another recompression zone occurs. Then, due to a slight decrease of the diameter, a low pressure zone is created before encountering the highly confined area where the boosters are linked to the main stage with the forward struts. Finally,

DOI: 10.13009/EUCASS2019-274

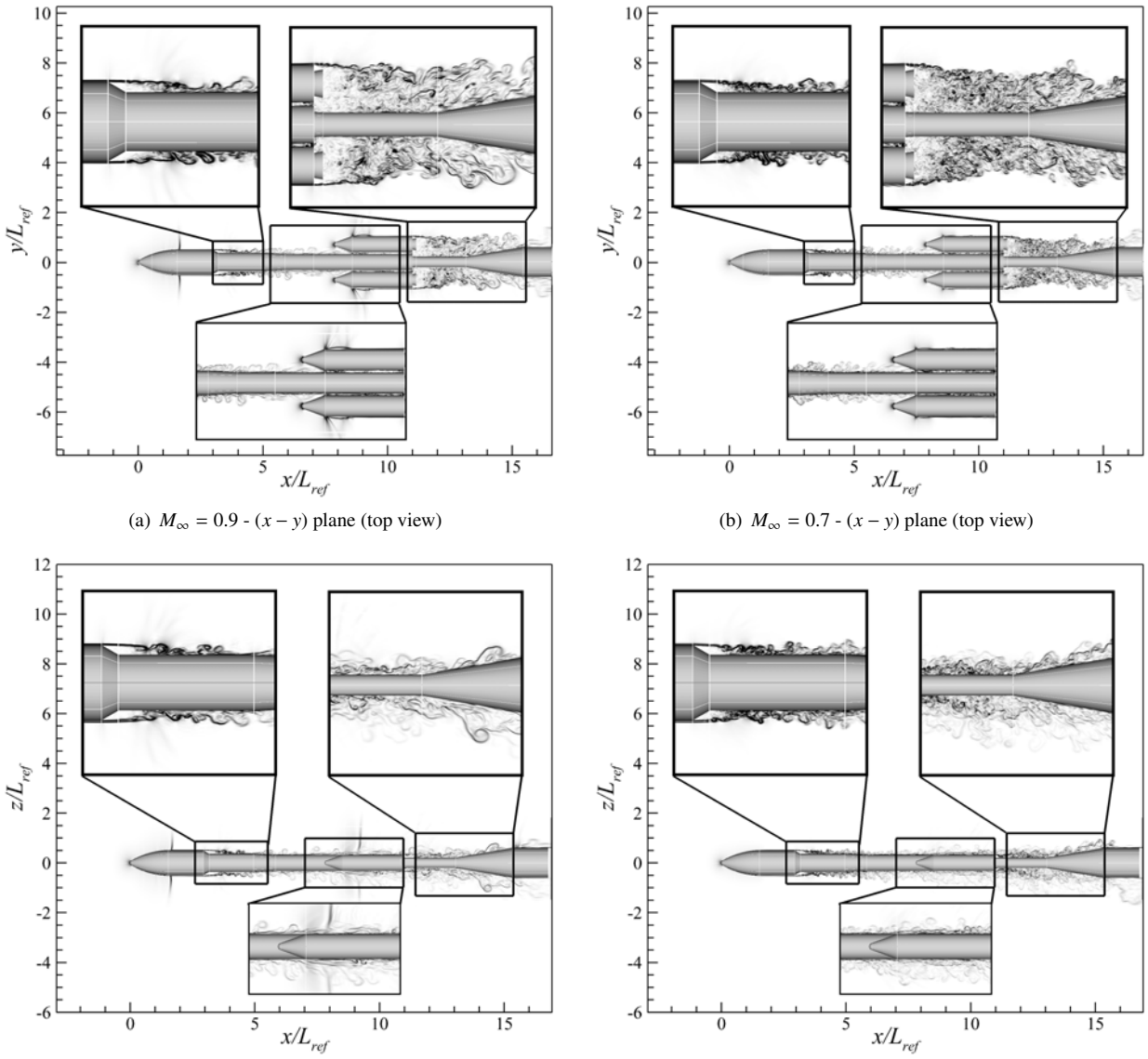

(a) $M_\infty = 0.9$ - $(x-y)$ plane (top view)

(b) $M_\infty = 0.7$ - $(x-y)$ plane (top view)

(c) $M_\infty = 0.9$ - $(x-z)$ plane (side view)

(d) $M_\infty = 0.7$ - $(x-z)$ plane (side view)

Figure 5: Iso-contours of the density gradient norm $\left(\left\|\overrightarrow{grad}\,\rho\right\|\right)$

the recirculation zone existing after the afterbody base constitutes a novel low pressure area. The main differences of $\overline{Cp}$ levels come from the shock wave located near the middle of the fairing and after the nose cones of the boosters. It seems that these normal shock waves contribute to a spatial extent of the high pressure zones.

6. Investigation of the fluctuating field

Despite the first-order statistics almost exhibit flow fields with a plane of symmetry namely $(x-z)$ for both Mach numbers of interest, it is not necessarily the case for the spatial organisation of the fluctuating pressure. The contours of the root-mean-square coefficient of the pressure fluctuation Cp_{rms} are represented at the wall for both Mach numbers in figure 8. This second order moment of the pressure time signal is defined as $Cp_{rms} = \overline{p'}/\frac{1}{2}\rho_\infty U_\infty^2$ where $\overline{p'}$ stands for the fluctuating pressure. For case M09 a strong asymmetry can be noticed comparing the highest *rms* pressure value patterns at the wall of the two boosters seen from the top. On the contrary, the fluctuating pressure signature at the wall for the two configurations M07 and M09 tends to remain symmetrical under the boosters (i.e. for negative z). Such a major difference between $M_\infty = 0.7$ and $M_\infty = 0.9$ suggests a very different flow dynamics for these two configurations in the transonic regime. Then, at the junction between the conical nose and the cylindrical body of the

DOI: 10.13009/EUCASS2019-274

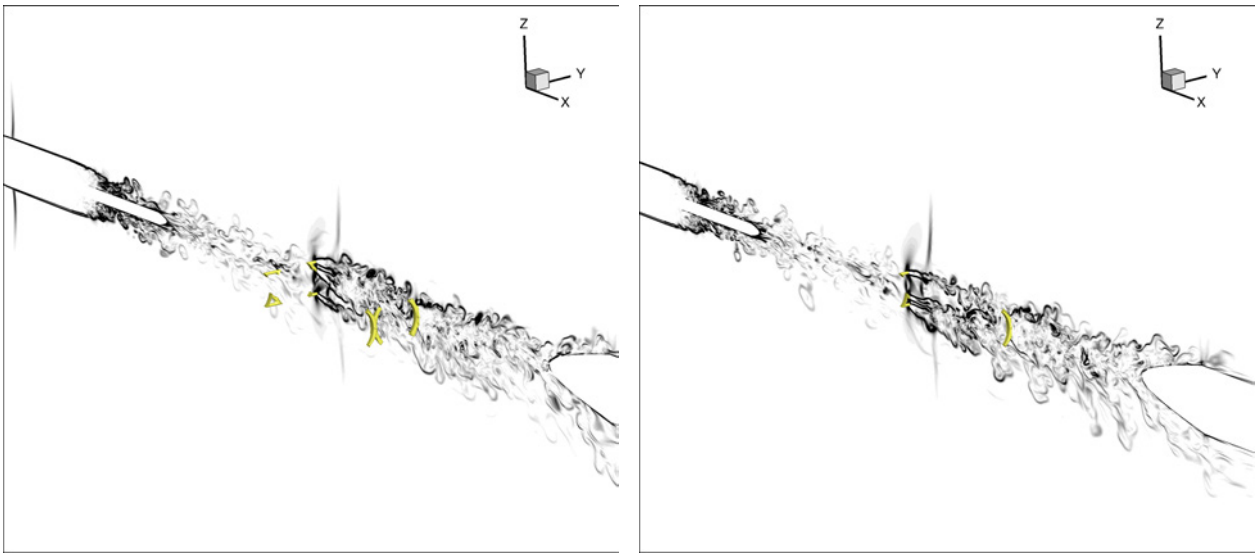

(a) $M_\infty = 0.9$ - plane between the main stage and the right booster

(b) $M_\infty = 0.9$ - plane between the main stage and the left booster

(c) $M_\infty = 0.7$ - plane between the main stage and the right booster

(d) $M_\infty = 0.7$ - plane between the main stage and the left booster

Figure 6: Iso-contours of the density gradient norm $\left(\left\|\overrightarrow{grad}\,\rho\right\|\right)$

boosters a strong oscillation of shock waves is unveiled by oblique patterns of high fluctuating pressure values at the wall. This oscillatory motion of the expansion and shock waves can be observed in the flow field in figure 9. Finally, the aft struts located at the edge of the afterbody base constitute a strong blockage effect for the incoming flow. Therefore, they encounter higher Cp_{rms} levels than to the forward struts linking the booster noses to the main body. The fact that the configuration presents very confined areas could explain the occurrence of unique unsteady phenomena leading to a flow mechanism clearly appearing at $M_\infty = 0.9$ which is close to a sonic Mach number and not for a lower transonic Mach number such as $M_\infty = 0.7$.

Figure 9 represents an isosurface approximately bounding the maximum values of Cp_{rms} which permits to identify the asymmetry behind the struts linking the booster noses in the flow field for the M09 case while the M07 case almost remains symmetrical. First, following the separation of the flow on the fairing, the signature of the fluctuating pressure field at the wall is characteristic of an axisymmetric backward facing step with levels ranging from 5 to 10% of the dynamic pressure.[8,36]

The reattachment point on the main stage behaves as an intermittency phenomenom after the axisymmetric shear

DOI: 10.13009/EUCASS2019-274

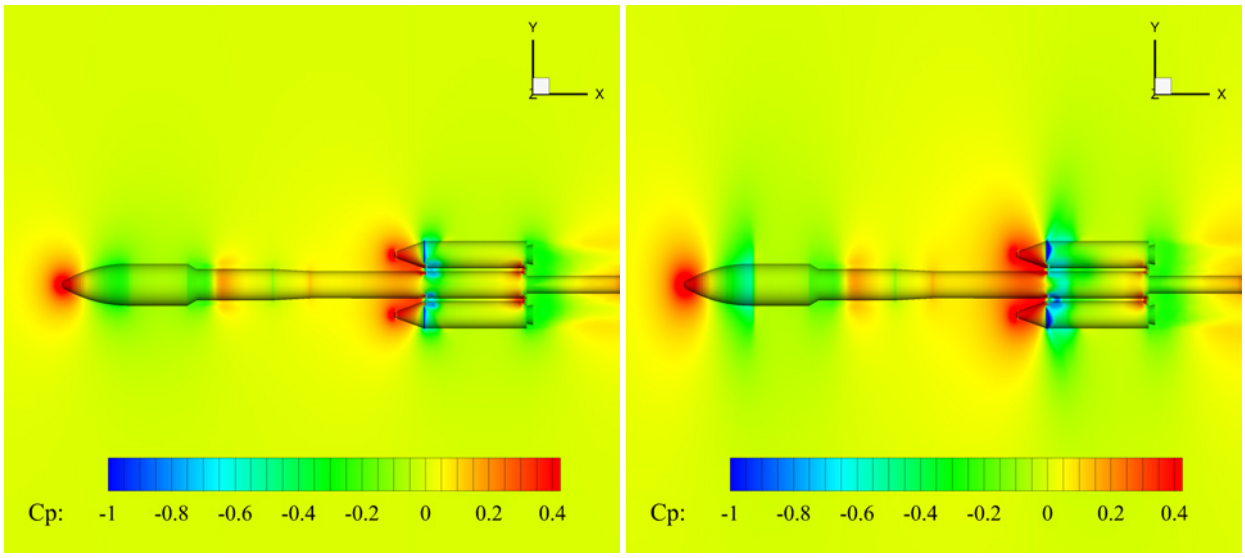

(a) $M_\infty = 0.7$ - $(x-y)$ plane (top view)

(b) $M_\infty = 0.9$ - $(x-y)$ plane (top view)

Figure 7: Iso-contours of the time-averaged pressure coefficient $\overline{Cp}$

layer impinges. Such a phenomenom also existing in the afterbody region encloses breathing recirculation bubbles.

These oscillatory motions potentially interact with the buffet of both the expansion waves and the shock waves located around the junction of the booster nose cones. The interaction of these unsteady phenomena occurs in highly confined areas with a strong blockage effect of the struts at the afterbody base. Then, it seems that when the flow becomes nearly sonic when the Mach number increases from $M_\infty = 0.7$ to $M_\infty = 0.9$ an instability with its own dynamics is generated.

7. Conclusion and perspectives

A sub-scale Ariane 6 PPH model with sting has been computed for two transonic Mach numbers (i.e. $M_\infty = 0.7$ and 0.9) with an angle of attack equal to $-3°$. Such a simulation has been achieved taking advantage of the coupling between ZDES and a zonal use of IBC. In particular, the M09 case exhibiting unsteady phenomena related to oscillating expansion and shock waves which occurs in a very confined area has permitted to demonstrate the robustness of the present numerical strategy (ZIBC). Then, the spatial organisation of the instantaneous, mean and fluctuating flowfield for the two Mach numbers of interest has been compared. It has been shown that the more the flow accelerates from a Mach number equal to 0.7 until 0.9, the more the planar symmetry of the pressure fluctuation signature at the wall observed in the booster plane tends to break.
In future work, the spectral content of the fluctuating field will be investigated to evidence the characteristic wavelengths of the main unsteady phenomena occurring in this massively separated flow and compared with the available experimental database.

8. Acknowledgments

The Centre National d'Etudes Spatiales (CNES) is particularly acknowledged for funding the numerical activities related to the afterbody cases with struts and with all technological details modelled using the ZIBC approach developed in the frame of the research project ALLIGATOR funded by ONERA.

References

[1] C. Benoit, S. Péron, and S. Landier. Cassiopee: a CFD pre- and post-processing tool. *Aerospace Science and Technology*, 45:272–243, 2015.

DOI: 10.13009/EUCASS2019-274

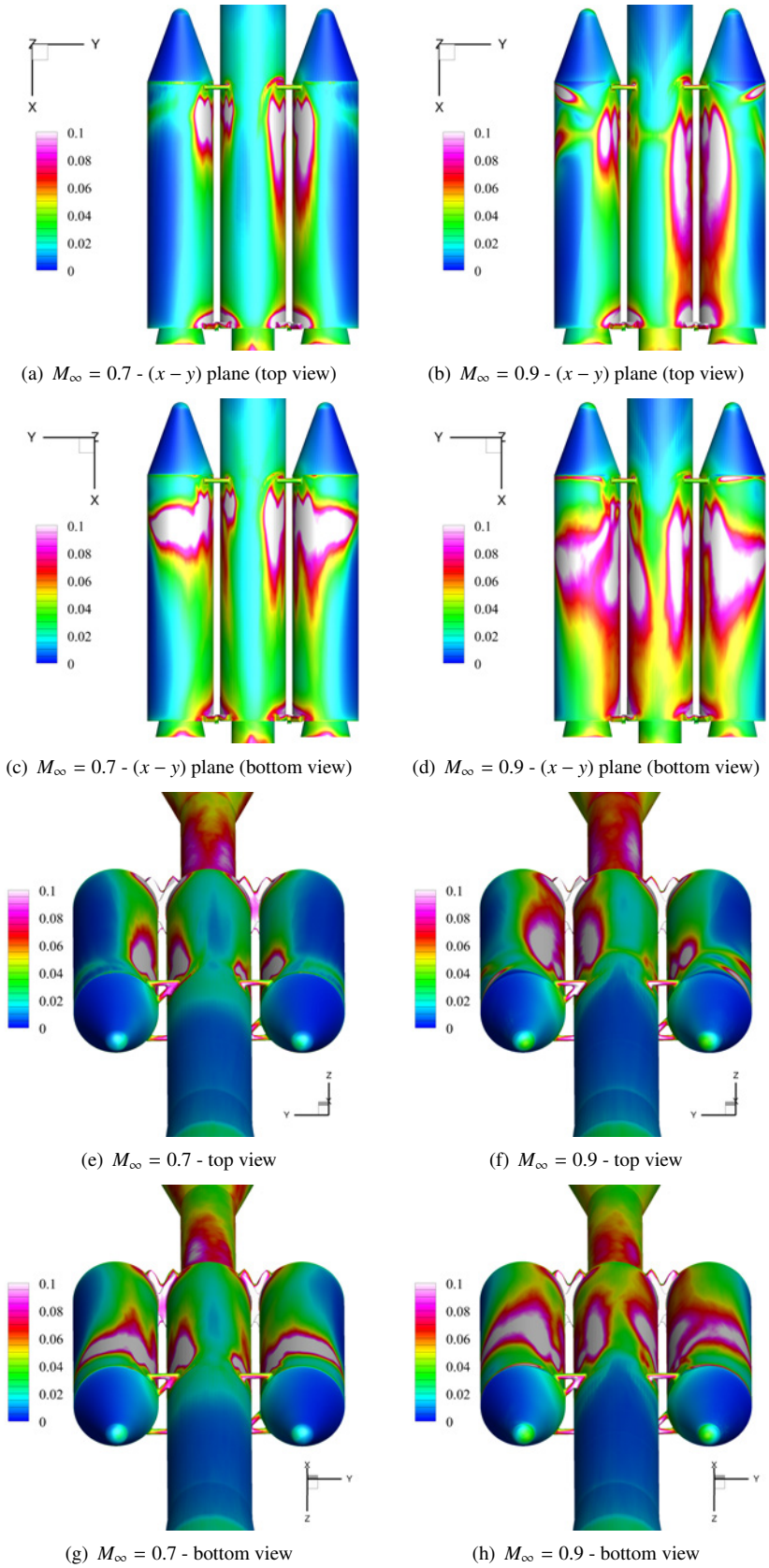

(a) M_∞ = 0.7 - $(x-y)$ plane (top view)

(b) M_∞ = 0.9 - $(x-y)$ plane (top view)

(c) M_∞ = 0.7 - $(x-y)$ plane (bottom view)

(d) M_∞ = 0.9 - $(x-y)$ plane (bottom view)

(e) M_∞ = 0.7 - top view

(f) M_∞ = 0.9 - top view

(g) M_∞ = 0.7 - bottom view

(h) M_∞ = 0.9 - bottom view

Figure 8: Spatial organisation of the fluctuating pressure coefficient Cp_{rms} at the wall for test cases $M07$ (top) and $M09$ (bottom)

DOI: 10.13009/EUCASS2019-274

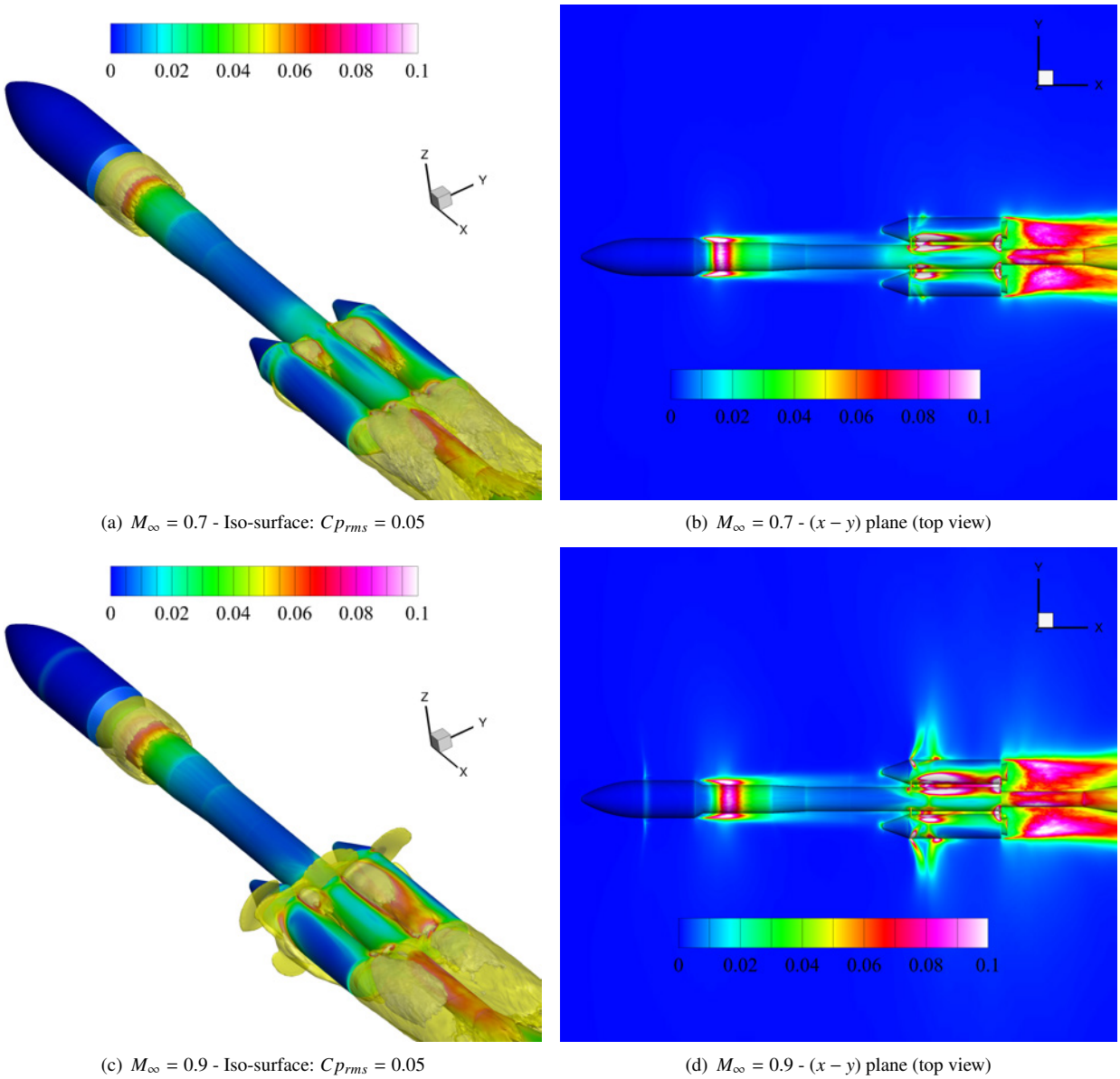

(a) $M_\infty = 0.7$ - Iso-surface: $Cp_{rms} = 0.05$

(b) $M_\infty = 0.7$ - $(x-y)$ plane (top view)

(c) $M_\infty = 0.9$ - Iso-surface: $Cp_{rms} = 0.05$

(d) $M_\infty = 0.9$ - $(x-y)$ plane (top view)

Figure 9: Spatial organisation of the fluctuating pressure coefficient Cp_{rms} in the flow field for the two Mach numbers

[2] L. Cambier, S. Heib, and S. Plot. The Onera elsA CFD Software: Input from Research and Feedback from Industry. *Mechanics and Industry*, 14(3):159,174, 2013.

[3] L. Charrier, M. Jubera, G. Pont, F. Grasso, S. Marié, and P. Brenner. Simulations of reactive supersonic/subsonic flow interactions for space launcher applications on FLUSEPA solver. *51st International Conference on Applied Aerodynamics, Strasbourg, France, 4 - 6 April*, 2016.

[4] S. David and S. Radulovic. Prediction of buffet loads on the ariane 5 afterbody. *6th International Symposium on Launcher Technologies, Munich, Germany, November*, 2005.

[5] S. Deck. Zonal-Detached-Eddy Simulation of the flow around a high-lift configuration. *AIAA Journal*, 43(11):2372–2384, November 2005.

[6] S. Deck. Recent improvements in the Zonal Detached Eddy Simulation (ZDES) formulation. *Theoretical and Computational Fluid Dynamics*, 26(6):523–550, December 2012.

[7] S. Deck, P. Duveau, P. d'Espiney, and P. Guillen. Development and application of Spalart-Allmaras one equation turbulence model to three-dimensional supersonic complex configurations. *Aerospace Science and Technology*, 6(3):171–183, 2002.

DOI: 10.13009/EUCASS2019-274

[8] S. Deck and P. Thorigny. Unsteadiness of an axisymmetric separating-reattaching flow. *Physics of Fluids*, 19(065103), 2007.

[9] S. Deck, P.-E. Weiss, and N. Renard. A rapid and low noise switch from RANS to WMLES on curvilinear grids with compressible flow solvers. *Journal of Computational Physics*, 363:231–255, 2018.

[10] E. A. Fadlun, R. Verzicco, P. Orlandi, and J. Mohd-Yusof. Combined Immersed-Boundary/Finite-Difference Methods for Three-Dimensional Complex Flow Simulations. *Journal of Computational Physics*, 161(1):35–60, 2000.

[11] E. G. M. Geurts. Steady and unsteady pressure measurements on the rear section of various configurations of the ariane 5 launch vehicle. *6th International Symposium on Launcher Technologies, Munich, Germany, November*, 2005.

[12] D. Goldstein, R. Handler, and L. Sirovich. Modeling a no-slip flow boundary with an external force field. *Journal of Computational Physics*, 105(2):354–366, 1993.

[13] P. Guillen and M. Dormieux. Design of a 3D multi-domain Euler code. In *International Seminar of Supercomputing*, Boston, USA, 1989.

[14] M.C. Lai and C.S. Peskin. An Immersed Boundary Method with Formal Second-Order Accuracy and Reduced Numerical Viscosity. *Journal of Computational Physics*, 160(2):705–719, 2000.

[15] M. S. Liou. A sequel to AUSM : AUSM+. *J. Comp. Phys.*, 129:364–382, 1996.

[16] L. Manueco, P. E. Weiss, and S. Deck. Towards the Prediction of Fluctuating Wall Quantities Using Immersed Boundary Conditions. *AIAA Aviation, Dallas, USA, 17-21 June*, 2019.

[17] R. Mittal and G. Iaccarino. Immersed boundary methods. *Annual Review of Fluid Mechanics*, 37:239–261, 2005.

[18] L. Mochel, P. E. Weiss, and S. Deck. Zonal Immersed Boundary Conditions: Application to a high Reynolds number afterbody flow. *AIAA Journal*, 52(12):2782–2794, 2014.

[19] J. Mohd-Yusof. Combined immersed-boundary/b-spline methods for simulations of flows in complex geometries. *Annual Research Briefs, Center for Turbulence Research*, pages 317–328, 1997.

[20] J. O'Rourke. Computational geometry in C, Second Edition. Cambridge University Press, 1998.

[21] R. Pain, P. E. Weiss, and S. Deck. Zonal Detached Eddy Simulation of the flow around a simplified launcher afterbody. *AIAA Journal*, 52:1967–1979, 2014.

[22] M. Péchier, P. Guillen, and R. Caysac. Magnus effect over finned projectiles. *AIAA Journal of Spacecraft and Rockets*, 38(4):542–549, 2001.

[23] C.S. Peskin. Flow Patterns Around Heart Valves: A Numerical Method. *Journal of Computational Physics*, 10(2):252–271, 1972.

[24] C.S. Peskin. The fluid dynamics of heart valves: Experimental, theoretical and computational methods. *Annual Review of Fluid Mechanics*, 14(1):235–259, 1982.

[25] G. Pont, D. Puech, M. Jubera, M. Dramont, and P. Brenner. CFD modeling of a space launch during the atmospheric phase. *50st International Conference on Applied Aerodynamics, Toulouse, France, 30 March - 1 April*, 2015.

[26] D. Saile, V. Kühl, and A. Gülhan. On the subsonic near-wake of a space launcher configuration without jet. *Experiments in Fluids*, 60(4), March 2019.

[27] R. Schwane. Numerical prediction and experimental validation of unsteady loads on ARIANE5 and VEGA. *Journal of Spacecraft and Rockets*, 52(1):54–62, January 2015.

[28] P. R. Spalart and S. R. Allmaras. A one equation turbulence model for aerodynamics flows. *La Recherche Aérospatiale*, (1):5–21, 1994.

[29] P.R. Spalart and S.R. Allmaras. A one equation turbulence model for aerodynamic flows. *La Recherche Aérospatiale*, pages 5 – 21, 1994.

DOI: 10.13009/EUCASS2019-274

[30] R. Verzicco, J. Mohd-Yusof, P. Orlandi, and D. Haworth. Large eddy simulation in complex geometric configurations using boundary body forces. *AIAA Journal*, 38(3):427–433, 2000.

[31] P. E. Weiss and S. Deck. Control of the antisymmetric mode ($m = 1$) for high Reynolds axisymmetric turbulent separating/reattaching flows. *Physics of Fluids*, 23(095102), 2011.

[32] P. E. Weiss and S. Deck. ZDES of the flow dynamics on an Ariane 5-type afterbody with and without struts. *6th European Conference for Aerospace Sciences, Flight Physics, Launcher Aerodynamics*, 2015.

[33] P. E. Weiss and S. Deck. Towards an efficient and robust numerical strategy for fast aerodynamic performance prediction on launch vehicles. *7th European Conference for Aerospace Sciences, Flight Physics, Launcher Aerodynamics*, 2017.

[34] P. E. Weiss and S. Deck. On the coupling of a zonal body-fitted/immersed boundary method with ZDES: application to the interactions on a realistic space launcher afterbody flow. *Computers & Fluids*, 176:338–352, 2018.

[35] P. E. Weiss, S. Deck, J.-C. Robinet, and P. Sagaut. On the dynamics of axisymmetric turbulent separating/reattaching flows. *Physics of Fluids*, 21:075103, 2009.

[36] P. E. Weiss, S. Deck, J. C. Robinet, and P. Sagaut. On the dynamics of axisymmetric turbulent separating/reattaching flows. *Physics of Fluids*, 21(075103), 2009.